JOURNAL OF COMPUTATIONAL PHYSICS 84, 441–460 (1989)

A Multistep Implicit Scheme for Time-Dependent 2-Dimensional Magnetohydrodynamic Flows

Y. Q. HU*

High Altitude Observatory, National Center for Atmospheric Research,†
P.O. Box 3000, Boulder, Colorado 80307

Received April 8, 1988; revised September 13, 1988

It is well known that many solar phenomena take place in or near active regions where the magnetic fields are so strong as to play a predominant role in supporting, heating, and accelerating the plasma. The time step would be severely restricted by the CFL condition and a long time computation would be subjected to numerical instability if an explicit method were adopted in these cases. In addition, improper treatment of the artificial boundaries one has to introduce in order to limit the size of the computational domain often leads to unphysical reflections. An implicit algorithm for solving time-dependent, 2-dimensional magnetohydrodynamic equations is presented which consists of a multistep implicit scheme for discretizing the governing equations and the projected characteristic method for stipulating artificial boundary conditions. The algorithm is illustrated by a physical problem concerning the dynamical response of the static atmosphere to a magnetic flux emergence of opposite polarity from below the photosphere. The stability criteria are given for both the scheme and the projected characteristic method.

I. INTRODUCTION

It is observed that a wide range of solar active phenomena are associated with in situ magnetic fields. The photosphere, especially in active regions, is subjected to ceaseless complex motions such as horizontal shearing, expanding, or squeezing, and vertical ejection as well. These motions change the magnetic flux distribution on the photosphere, thereby causing a variation of both the magnetic configuration and the plasma structure in the solar atmosphere. Extensive numerical studies have been carried out to explore these phenomena and their influences on the solar atmosphere and interplanetary medium. For transient phenomena characterized by various waves, explicit schemes are preferred since the CFL condition does not impose a severe restriction on the time step and the physical time of computation is always taken to be nearly that for the fast wave to travel through the domain. On the contrary, for those phenomena evolving slowly with time compared to wave motions, one is mainly interested in the structural evolutions and mass motions of plasma, and thus implicit methods are required to procure a high stability for long time computation. Here "long time" means that it is longer or much longer than the

* Permanent address: University of Science and Technology of China, Hefei, Anhui, China.
† The National Center for Atmospheric Research is sponsored by the National Science Foundation.

0021-9991/89 $3.00

above-mentioned travelling time of the fast wave. Usually an implicit method requires more computer time for each time step. Both an increase of the time step and a reduction of the computational expense of each step have been attempted by various sophisticated implicit techniques, among which are the implicit-continuous-Eulerian (ICE) scheme by Harlow and Amsden [1, 2] and the alternating direction implicit (ADI) scheme (e.g., Lindemuth and Killeen [3]; Schnack and Killeen [4]). In order to analyze the atmospheric response to very slow motions (~ 1 km/s) of the photosphere we proposed the FICE scheme (Hu and Wu [5]). This is an extension of the ICE method and includes non-reflecting conditions based on the projected characteristic method. The FICE scheme has been successfully applied to the dynamics of the solar atmosphere associated with subsonic disturbances on the photosphere (e.g., Wu *et al.* [6–9]). However, this scheme does not work well for lower values of β (the ratio of gas pressure to magnetic pressure) because it is mainly based on an implicit treatment of gas pressure, which poorly reflects the predominant role of the magnetic field.

In the present paper we will propose a multistep implicit algorithm which is applicable to time-dependent, 2-dimensional MHD flows in a strong magnetic field. Because of the implicit treatment, phenomena occurring in the time scale of the fast mode are somewhat smoothed, but the method allows us to study for the first time the slower structural evolutions of the plasma in strong field case. In Section 2, the 2-dimensional ideal MHD equations are cast in a form with the magnetic flux function as a dependent variable and are then discretized in terms of a 3-step implicit scheme. The techniques for using the projected characteristic method to specify the boundary conditions are given in Section 3. Finally, an example concerning the atmospheric response to a magnetic flux emergence from below the photosphere into a pre-existing bipolar background field of opposite polarity is presented to illustrate some interesting features of the algorithm. The algorithm is applicable to nonideal MHD cases, though we use an ideal MHD model for the example.

II. Governing Equations and ADI Scheme

For 2-dimensional problems in spherical coordinates we may introduce the magnetic flux function $\psi(t, r, \theta)$, defined by

$$\mathbf{B} = \frac{1}{r^2 \sin\theta}\frac{\partial\psi}{\partial\theta}\hat{r} - \frac{1}{r\sin\theta}\frac{\partial\psi}{\partial r}\hat{\theta}, \tag{1}$$

where r is the radius and θ the polar angle. Then the governing equations for ideal MHD flows can be expressed in the form

$$\frac{\partial\rho}{\partial t} + v_r\frac{\partial\rho}{\partial r} + \frac{v_\theta}{r}\frac{\partial\rho}{\partial\theta} + \rho\frac{\partial v_r}{\partial r} + \frac{\rho}{r}\frac{\partial v_\theta}{\partial\theta} + \frac{2\rho v_r}{r} + \frac{\rho v_\theta}{r}\cot\theta = 0, \tag{2.1}$$

$$\frac{\partial v_r}{\partial t} + v_r\frac{\partial v_r}{\partial r} + \frac{v_\theta}{r}\frac{\partial v_r}{\partial\theta} + \frac{RT}{\rho}\frac{\partial\rho}{\partial r} + R\frac{\partial T}{\partial r} + \frac{L\psi}{\rho}\frac{\partial\psi}{\partial r} - \frac{v_\theta^2}{r} + \frac{GM}{r^2} = 0, \tag{2.2}$$

$$\frac{\partial v_\theta}{\partial t}+v_r\frac{\partial v_\theta}{\partial r}+\frac{v_\theta}{r}\frac{\partial v_\theta}{\partial \theta}+\frac{RT}{\rho r}\frac{\partial \rho}{\partial \theta}+\frac{R}{r}\frac{\partial T}{\partial \theta}+\frac{L\psi}{\rho r}\frac{\partial \psi}{\partial \theta}+\frac{v_r v_\theta}{r}=0, \tag{2.3}$$

$$\frac{\partial \psi}{\partial t}+v_r\frac{\partial \psi}{\partial r}+\frac{v_\theta}{r}\frac{\partial \psi}{\partial \theta}=0, \tag{2.4}$$

$$\frac{\partial T}{\partial t}+v_r\frac{\partial T}{\partial r}+\frac{v_\theta}{r}\frac{\partial T}{\partial \theta}+(\gamma-1)\left[T\frac{\partial v_r}{\partial r}+\frac{T}{r}\frac{\partial v_\theta}{\partial \theta}+\frac{2Tv_r}{r}+\frac{Tv_\theta}{r}\cot\theta\right]=0, \tag{2.5}$$

where ρ is the density, v_r and v_θ are the velocity components, T is the temperature, R, G, M, and γ are the gas and Newton's constants, the mass of the sun, and the polytropic index, respectively, and the operator

$$L=\frac{1}{4\pi r^2\sin^2\theta}\left[\frac{\partial^2}{\partial r^2}+\frac{1}{4\pi r^2}\frac{\partial^2}{\partial \theta^2}-\frac{\cot\theta}{r^2}\frac{\partial}{\partial \theta}\right]. \tag{3}$$

Note that R has been doubled so as to include the contribution of electrons to the gas pressure. The introduction of ψ has the advantage of reducing by one the number of equations to be solved and guarantees the divergence-free condition while changing the magnetic flux distribution on the photosphere.

The set of MHD equations (2) may be rewritten as

$$\frac{\partial U}{\partial t}+W\left(U,\frac{\partial U}{\partial r},\frac{\partial U}{\partial \theta},\frac{\partial^2 U}{\partial r^2},\frac{\partial^2 U}{\partial \theta^2}\right)=0, \tag{4}$$

where $U=(\rho, v_r, v_\theta, \psi, T)$ is the vector of dependent variables, and the expression for the vector W may be derived in a straightforward way and is omitted for conciseness.

The proposed scheme is implemented in three steps. The first two steps correspond to the r-direction and θ-direction split-implicit treatment of Eq. (4) similar to that of Lindemuth and Killeen [3] but with a different coordinate system. In the following, a superscript n and subscripts i and j will refer to the point (t^n, r_i, θ_j) in the space-time mesh. For the first step, Eq. (4) reads

$$\frac{\bar{U}_{ij}^{n+1}-U_{ij}^n}{\Delta t}+\bar{W}_{ij}^{n+1}=0, \tag{5}$$

where a bar over the top denotes intermediate quantities, and

$$\begin{aligned}\bar{W}_{ij}^{n+1}=W^n&+\left(\frac{\partial W}{\partial U}\right)^n[\bar{U}^{n+1}-U^n]\\&+\left(\frac{\partial W}{\partial(\partial U/\partial r)}\right)^n\left[\left(\frac{\partial \bar{U}}{\partial r}\right)^{n+1}-\left(\frac{\partial U}{\partial r}\right)^n\right]\\&+\left(\frac{\partial W}{\partial(\partial^2 U/\partial r^2)}\right)^n\left[\left(\frac{\partial^2 \bar{U}}{\partial r^2}\right)^{n+1}-\left(\frac{\partial^2 U}{\partial r^2}\right)^n\right].\end{aligned} \tag{6}$$

Here the subscripts i and j are expressly implied for all quantities on the right-hand side. With the use of a central difference approximation for all the derivatives with respect to r at t^{n+1}, we can write the final difference expression of Eq. (5) as

$$A_{ij}\bar{U}_{ij}^{n+1}+B_{ij}\bar{U}_{i+1,j}^{n+1}+C_{ij}\bar{U}_{i-1,j}^{n+1}=E_{ij}, \tag{7}$$

where A_{ij}, B_{ij}, and C_{ij} are 5×5 matrices, and E_{ij} vectors, given by

$$A_{ij}=\frac{I}{\Delta t}+\left(\frac{\partial W}{\partial U}\right)_{ij}^{n}-\frac{2}{\Delta r_{i+1/2}\,\Delta r_{i-1/2}}\left(\frac{\partial W}{\partial(\partial^2 U/\partial r^2)}\right)_{ij}^{n}, \tag{8}$$

$$B_{ij}=\frac{1}{\Delta r_i\,\Delta r_{i+1/2}}\left(\frac{\partial W}{\partial(\partial^2 U/\partial r^2)}\right)_{ij}^{n}+\frac{1}{2\Delta r_i}\left(\frac{\partial W}{\partial(\partial U/\partial r)}\right)_{ij}^{n}, \tag{9}$$

$$C_{ij}=\frac{1}{\Delta r_i\,\Delta r_{i-1/2}}\left(\frac{\partial W}{\partial(\partial^2 U/\partial r^2)}\right)_{ij}^{n}-\frac{1}{2\Delta r_i}\left(\frac{\partial W}{\partial(\partial U/\partial r)}\right)_{ij}^{n}, \tag{10}$$

$$E_{ij}=-W_{ij}^{n}+\left[\frac{I}{\Delta t}+\left(\frac{\partial W}{\partial U}\right)_{ij}^{n}\right]U_{ij}^{n}+\left(\frac{\partial W}{\partial(\partial U/\partial r)}\right)_{ij}^{n}\left(\frac{\partial U}{\partial r}\right)_{ij}^{n}+\left(\frac{\partial W}{\partial(\partial^2 U/\partial r^2)}\right)_{ij}^{n}\left(\frac{\partial^2 U}{\partial r^2}\right)_{ij}^{n}. \tag{11}$$

Here I is the unit matrix and

$$\Delta r_i=\tfrac{1}{2}(r_{i+1}-r_{i-1}),\qquad \Delta r_{i+1/2}=r_{i+1}-r_i,\qquad \Delta r_{i-1/2}=r_i-r_{i-1}. \tag{12}$$

Similar notation is used for $\Delta\theta_j$ and $\Delta\theta_{j\pm 1/2}$.

For the second step, Eq. (4) becomes

$$\frac{\bar{U}_{ij}^{n+2}-\bar{U}_{ij}^{n+1}}{\Delta t}+\bar{W}_{ij}^{n+2}=0, \tag{13}$$

where

$$\begin{aligned}\bar{W}_{ij}^{n+2}=\bar{W}^{n+1}&+\left(\frac{\partial\bar{W}}{\partial\bar{U}}\right)^{n+1}[\bar{U}^{n+2}-\bar{U}^{n+1}]\\&+\left(\frac{\partial\bar{W}}{\partial(\partial\bar{U}/\partial\theta)}\right)^{n+1}\left[\left(\frac{\partial\bar{U}}{\partial\theta}\right)^{n+2}-\left(\frac{\partial\bar{U}}{\partial\theta}\right)^{n+1}\right]\\&+\left(\frac{\partial\bar{W}}{\partial(\partial^2\bar{U}/\partial\theta^2)}\right)^{n+1}\left[\left(\frac{\partial^2\bar{U}}{\partial\theta^2}\right)^{n+2}-\left(\frac{\partial^2\bar{U}}{\partial\theta^2}\right)^{n+1}\right].\end{aligned} \tag{14}$$

Similarly, the subscripts i and j for all quantities are expressly implied on the right-hand side. The final difference expression of Eq. (13) is

$$A'_{ij}\bar{U}_{ij}^{n+2}+B'_{ij}\bar{U}_{i,j+1}^{n+2}+C'_{ij}\bar{U}_{i,j-1}^{n+2}=E'_{ij}, \tag{15}$$

where A'_{ij}, B'_{ij}, and C'_{ij} are 5×5 matrices, and E'_{ij} vectors, given by

$$A'_{ij}=\frac{I}{\Delta t}+\left(\frac{\partial \bar{W}}{\partial \bar{U}}\right)^{n+1}_{ij}-\frac{2}{\Delta\theta_{j+1/2}\,\Delta\theta_{j-1/2}}\left(\frac{\partial \bar{W}}{\partial(\partial^2\bar{U}/\partial\theta^2)}\right)^{n+1}_{ij}, \tag{16}$$

$$B'_{ij}=\frac{1}{\Delta\theta_j\,\Delta\theta_{j+1/2}}\left(\frac{\partial \bar{W}}{\partial(\partial^2\bar{U}/\partial\theta^2)}\right)^{n+1}_{ij}+\frac{1}{2\Delta\theta_j}\left(\frac{\partial \bar{W}}{\partial(\partial\bar{U}/\partial\theta)}\right)^{n+1}_{ij}, \tag{17}$$

$$C'_{ij}=\frac{1}{\Delta\theta_j\,\Delta\theta_{j-1/2}}\left(\frac{\partial \bar{W}}{\partial(\partial^2\bar{U}/\partial\theta^2)}\right)^{n+1}_{ij}-\frac{1}{2\Delta\theta_j}\left(\frac{\partial \bar{W}}{\partial(\partial\bar{U}/\partial\theta)}\right)^{n+1}_{ij}, \tag{18}$$

$$E'_{ij}=-\bar{W}^n_{ij}+\left[\frac{I}{\Delta t}+\left(\frac{\partial \bar{W}}{\partial \bar{U}}\right)^{n+1}_{ij}\right]\bar{U}^{n+1}_{ij}+\left(\frac{\partial \bar{W}}{\partial(\partial\bar{U}/\partial\theta)}\right)^{n+1}_{ij}\left(\frac{\partial \bar{U}}{\partial\theta}\right)^{n+1}_{ij}+\left(\frac{\partial \bar{W}}{\partial(\partial^2\bar{U}/\partial\theta^2)}\right)^{n+1}_{ij}\left(\frac{\partial^2\bar{U}}{\partial\theta^2}\right)^{n+1}_{ij}, \tag{19}$$

An additional third step, which Lindemuth and Killeen did not have in their version, is to take an arithmetic average between U^n and $\bar{U}^{n+2}$ to get U^{n+1} for the new time step, namely,

$$U^{n+1}=\tfrac{1}{2}(U^n+\bar{U}^{n+2}). \tag{20}$$

This step will smooth the numerical solution, and such a smoothing technique was sometimes applied to multistep explicit schemes. Here we use it mainly for combining the r-direction and the θ-direction implicit treatments in each single time step. Although computer time is doubled and more numerical diffusion is introduced due to this step, we argue that it enhances the stability of long time computation and reduces the ripples in the numerical results, both of which appear to come from the nonlinear terms in Eqs. (2.2) and (2.3) associated with ψ.

To avoid the computational difficulties resulting from a finite difference treatment of steep gradients or strong shock waves, we introduce the following artificial diffusion, similar to Lapidus smoothing [10], into the left-hand side of Eq. (4)

$$W'=-D\cdot\max\left(\left|\frac{\partial v_r}{\partial r}\right|,\left|\frac{1}{r}\frac{\partial v_r}{\partial\theta}\right|,\left|\frac{\partial v_\theta}{\partial r}\right|,\left|\frac{1}{r}\frac{\partial v_\theta}{\partial\theta}\right|\right)\left(\Delta r^2\frac{\partial^2 U}{\partial r^2}+\Delta\theta^2\frac{\partial^2 U}{\partial\theta^2}\right), \tag{21}$$

where D is a diagonal matrix, with elements d_i ($i=1,\ldots,5$). The d_i are the dimensionless coefficients of artificial diffusion for ρ, v_r, v_θ, ψ, and T, respectively, which are usually taken to be the same value. In principle, the smaller the d_i the better as long as the algorithm remains stable. Also, the d_i need not all be equal, and it is found that the diffusion added to v_r and v_θ appears to be more important for numerical stability than the others. In our computation we took $d_2=d_3=2$, whereas $d_1=d_5=0.5$ and $d_4=0$. The latter means that no artificial diffusion is added to ψ. Tests show that diffusion in ψ has little influence on the numerical

stability, but does lead to deformation of the magnetic configuration via magnetic resistivity. Incidently, the artificial diffusion terms W' are treated implicitly along with W.

III. Boundary Conditions

The treatment of boundary conditions has long been a formidable issue in numerical studies. We have previously developed a projected characteristic method, which was incorporated into the FICE scheme, to specify boundary conditions [5]. This method is independent of any difference schemes to be adopted and will be applied to the present scheme.

Let us briefly review the basic idea of the projected characteristic method. According to this method, the characteristics for an arbitrary set of hyperbolic partial differential equations are first projected to the n–t plane, where n is the unit normal to the boundary in question. Then these projected characteristics are classified in two parts: outgoing and incoming, depending on whether they go out of or come into the domain of solution from the boundary. As a rule, the number of quantities to be arbitrarily specified on the boundary should not exceed the number of incoming characteristics, whereas the unspecified quantities must satisfy compatibility relations along the outgoing characteristics. This is the case for a physical boundary. For an artificial boundary introduced merely for limiting the domain, however, no quantities can be arbitrarily specified. Instead, a new set of non-reflecting conditions are constructed by discarding all terms in the projected characteristic equations along the incoming characteristics except for those with temporal derivatives. Finally, the non-reflecting conditions are combined with the compatibility relations so as to determine all dependent variables on the boundary.

We will follow the procedures described by Hu and Wu [5] to stipulate the boundary condition for the present problem. Suppose the domain of solution is defined by

$$r_0 \leqslant r \leqslant r_m, \qquad \theta_0 \leqslant \theta \leqslant \frac{\pi}{2}, \tag{22}$$

for which there are four boundaries: the bottom ($r = r_0$) is a physical boundary, the left side ($\theta = \theta_0$) and the top ($r = r_m$) are artificial, and the right side ($\theta = \pi/2$) is symmetrical (cf. Fig. 1). The formulation of the projected characteristics and their associated characteristic equations is included in the Appendix. A summary of the boundary conditions and their discrete forms are described below.

For the left side and the top, we use the non-reflecting boundary conditions along incoming characteristics and the compatibility relations along outgoing ones to explicitly determine the boundary values (cf. Appendix). In order to maintain the

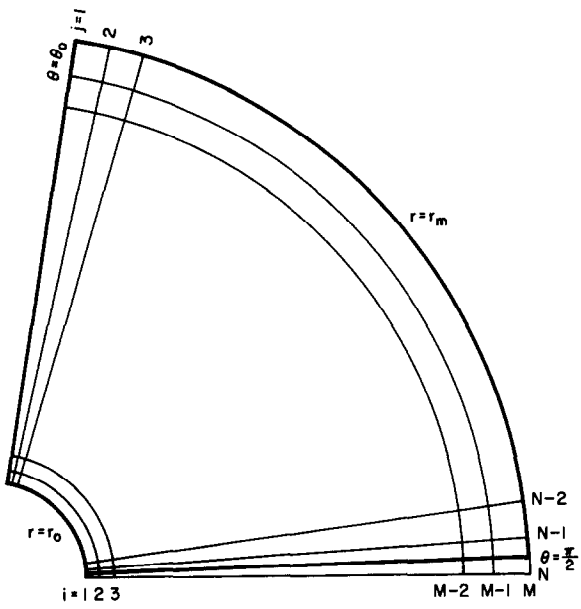

FIG. 1. Computational domain and mesh.

numerical stability and accuracy the following CFL condition should be observed on these boundaries:

$$\Delta t < \Delta t_1 = \min\left(\frac{\Delta l}{|v_n| + c_s}\right), \tag{23}$$

where Δl is the normal grid spacing, $c_s = \sqrt{\gamma RT}$ the sound speed, and v_n the normal velocity. This limitation is not critical considering that the local Alfven speed, which is high for a strong magnetic field, does not appear in the denominator.

Next we displace the right side a half-grid spacing from $\theta = \pi/2$, as shown in Fig. 1. Then the symmetry condition on it is simply that

$$\begin{gathered} \rho_{i,N-1} = \rho_{i,N}, \qquad v_{ri,N-1} = v_{ri,N}, \qquad v_{\theta i,N-1} = -v_{\theta i,N}, \\ \psi_{i,N-1} = \psi_{i,N}, \qquad T_{i,N-1} = T_{i,N}, \end{gathered} \tag{24}$$

where θ_N lies at $\theta = \pi/2 + 1/2\,\Delta\theta$.

Finally, the bottom is considered as a physical boundary on which some dependent variables are properly prescribed as functions of time to represent a specific disturbance. There are a lot of alternatives to do so in principle. In the example given in the next section, the bottom is divided into an ejective region and a quiet region. In the ejective region all dependent variables are specified for simplicity no matter what the normal ejective speed is, whereas for the quiet region, we

observe the rule of the projected characteristic method mentioned above, namely, specify only three of the five quantities, for instance, v_r, v_θ, and ψ, and leave two others, ρ and T, determined by compatibility relations. In this case, condition (23) ought to be observed.

To discretize the compatibility relations on a boundary, an inward difference is utilized for all normal derivatives whereas a central difference is used for the tangential derivatives. To reduce the differencing error in the Lorentz force term, which is crucial for a plasma in a strong magnetic field, specific attention is paid to the difference approximation of $L\psi$. At the left side, for instance, we use

$$(L\psi)_{i,1} = \frac{\psi_{i+1,2} + \psi_{i-1,2} - 2\psi_{i,2}}{\Delta r_i^2} + \frac{\psi_{i,3} + \psi_{i,1} - 2\psi_{i,2}}{r_i^2 \, \Delta\theta^2} - \frac{\cot\theta}{2r_i^2 \, \Delta\theta}(\psi_{i,3} - \psi_{i,1}), \tag{25}$$

in which all the differences are referred to the same point $(i, 2)$. Expression (25) has a formal accuracy of second order for $(L\psi)_{i,2}$. Practical experience shows that as long as the electric current density is not very large on the boundary, taking $(L\psi)_{i,1} \approx (L\psi)_{i,2}$ is acceptable and better than using an inward difference directly at the boundary point $(i, 1)$.

IV. Numerical Example

In this section the present algorithm is illustrated by a physical problem concerning the dynamical response of the static atmosphere to a magnetic flux emergence of opposite polarity from below the solar surface. A similar problem has been treated analytically in terms of a low-β approximation [11] and numerically in Cartesian coordinates [12]. Although the calculation to be presented is a natural continuation of the above-mentioned work, it is not an attempt to model a real solar phenomenon. Rather, it is intended to display the basic physical features of the interaction between plasma and magnetic field and to suggest the use of this algorithm for future calculations dealing with solar phenomena controlled by magnetic fields.

1. *Computational Domain and Mesh*

For the calculations reported in this paper, the domain of solution is taken to be $R_\odot \leqslant r \leqslant 6R_\odot$ ($R_\odot$ is the solar radius) and $12° \leqslant \theta \leqslant 92°$, and subdivided into a 30×21 mesh, 30 points in the r-direction and 21 in the θ-direction. The grid points are equally spaced in the θ-direction with $\Delta\theta = 4°$ but have an increasing spacing with the radial distance in the r-direction according to

$$\Delta r_{i+1} = (1 + \delta)\, \Delta r_i, \tag{26}$$

where $\delta = \Delta r_1 / R_\odot = 0.0637$. Note that the equator ($\theta = 90°$) is located at a half-grid point as previously stated.

2. *Initial and Boundary Conditions*

The initial solar atmosphere is assumed to be in isothermal hydrostatic equilibrium, permeated by a potential magnetic field. The analytical initial conditions are given by

$$\begin{aligned}
&\rho_0 = \rho_c \exp\left[-\frac{GM}{RTR_\odot}\left(1 - \frac{R_\odot}{r}\right)\right],\\
&T_0 = T_c,\\
&v_0 = 0,\\
&\psi_0 = \frac{\psi_c}{R_\odot}\left(r(1-g^2)\left[(1+f^2)\tan^{-1}\frac{1}{f} - f\right] - \frac{\pi a^2 \sin^2\theta}{2r} + 2ah\right),
\end{aligned} \tag{27}$$

where ρ_c, T_c, ψ_c, and a are arbitrary constants, and

$$\begin{aligned}
f^2 &= -\frac{1}{2}\left(1 - \frac{a^2}{r^2}\right) + \frac{1}{2}\left[\left(1 - \frac{a^2}{r^2}\right)^2 + \frac{4a^2}{r^2}\cos^2\theta\right]^{1/2},\\
g^2 &= \frac{1}{2}\left(1 - \frac{a^2}{r^2}\right) + \frac{1}{2}\left[\left(1 - \frac{a^2}{r^2}\right)^2 + \frac{4a^2}{r^2}\cos^2\theta\right]^{1/2},\\
h^2 &= \frac{r^2}{a^2} f^2.
\end{aligned}$$

The expression for ψ_0 comes from Low [13] and represents a potential field with a neutral current sheet at the equation from $r = a$ to infinity, as shown in Fig. 2a.

A flux emergence of opposite polarity accompanied with a mass ejection is introduced across the equator with $\theta = \theta_c$ as the edge of the ejective region on the solar surface, within which we set

$$\begin{aligned}
&v_r = \frac{v_c(\sin^2\theta - \sin^2\theta_c)}{\sin^2\theta\cos^2\theta_c},\\
&v_\theta = 0,\\
&\psi = \psi(0, r_0, \theta)\exp\left(\frac{v_r t}{r_0}\right), \qquad \text{if} \quad \psi \geqslant \psi\left(0, r_0, \frac{\pi}{2}\right)\\
&\quad = 2\psi\left(0, r_0, \frac{\pi}{2}\right) - \psi(0, r_0, \theta)\exp\left(\frac{v_r t}{r_0}\right), \qquad \text{if} \quad \psi < \psi\left(0, r_0, \frac{\pi}{2}\right)\\
&\rho = \rho_c\left(1 + \frac{\alpha v_r}{v_c}\right),\\
&T = \frac{\rho_c}{\rho} T_c,
\end{aligned} \tag{28}$$

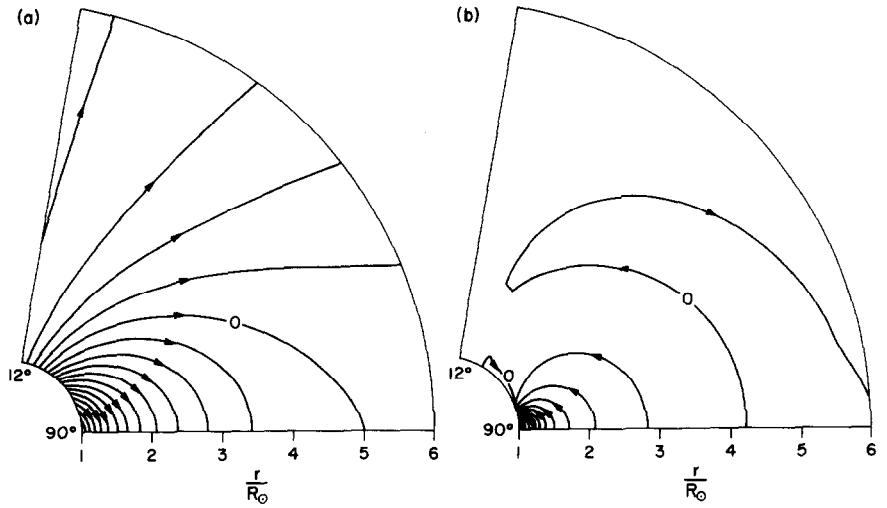

FIG. 2. Magnetic configuration (contours of ψ) at (a) 0 s and (b) 16,000 s.

where v_c and α are constants, $r_0 = R_\odot$. As Eqs. (28) show, the velocity and the enhanced density are turned on abruptly at $t = 0$ and kept constant thereafter. Meantime, the gas pressure at the boundary is held fixed throughout the calculation. The velocity distribution at $t \geqslant 0$ is schematically shown in the upper part of Fig. 3. The same figure also shows the magnetic flux distribution in accordance with Eq. (28), with curve $ABD'FG$ at $t = 0$ and curve $ABCDEFG$ at a certain time $t > 0$. Note that curve CDE is the image of curve $CD''E$ with respect to horizontal line

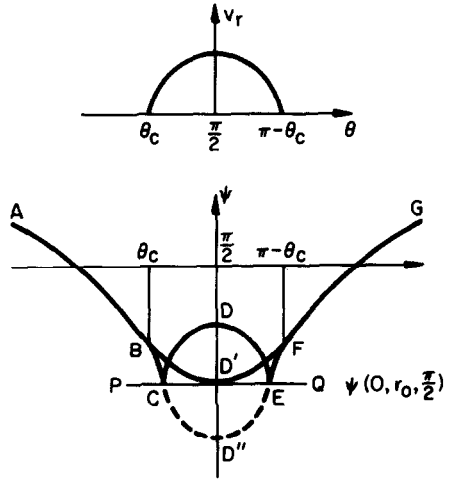

FIG. 3. The ejective velocity and disturbed magnetic flux distribution in the ejective region on the solar surface ($r_0 = R_\odot$).

PQ, and that the height of $D'D$ increases exponentially with time as can be seen from Eq. (28). Obviously, C and E are the border of an emerging magnetic field structure which has a polarity opposite to that of the background field outside. As for the quiet region we keep v_r and v_θ vanishing and ψ invariant and leave ρ and T determined by pertinent compatibility relations. This entire specification is somewhat arbitrary but seems to approximately reflect some observations of photospheric ejections (e.g., Rust [14]; Uchida and Sakurai [15]).

In the following computation, the relevant constants are

$$\rho_c = 1.67 \times 10^{-16}\ \text{g/cm}^3, \qquad T_c = 1.5 \times 10^6\ K,$$
$$v_c = \sqrt{RT} = 160\ \text{km/s}, \qquad \theta_c = 72°, \qquad \alpha = 3, \qquad \gamma = 1.1, \tag{29}$$
$$a = 5R_\odot, \qquad \psi_c = 1.211 \times 10^{20}\ mx,$$

which implies a subsonic ejection with $\beta \approx 1$ (correspondingly the Alfven speed $v_a \approx 230$ km/s) initially at the equator. Note that the minimum value of β will decrease nearly exponentially with time to about 1.66×10^{-4} and v_a will reach a maximum $\sim 6 \times 10^3$ km/s at 16000 s. The other boundary conditions have been described already in Section 3.

3. Numerical Results

Figures 4 through 6 show the distributions of density enhancement, temperature enhancement, and velocity at several separate times, respectively, and Fig. 2b depicts the magnetic configuration at $t = 16{,}000$ s. From these figures, we clearly see a high density loop is formed in the neutral current sheet region between the newly emerging magnetic field and the background. The maximum density within the loop

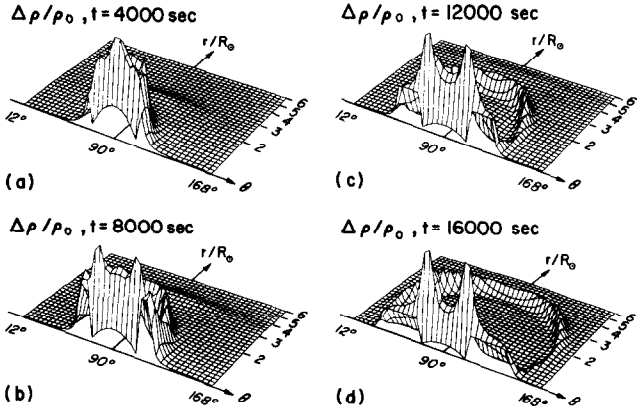

FIG. 4. Density enhancement at (a) 4000 s, (b) 8000 s, (c) 12,000 s, and (d) 16,000 s. The value at $r = R_\odot$, $\theta = \pi/2$ is identically equal to 3.

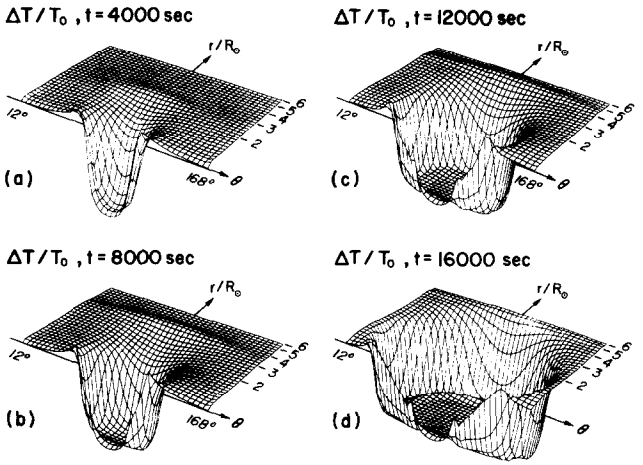

FIG. 5. Temperature enhancement at (a) 4000 s, (b) 8000 s, (c) 12,000 s, and (d) 16,000 s. The value at $r = R_{\odot}$, $\theta = \pi/2$ is identically equal to -0.75.

is eight times higher than the background, as shown in Figs. 4a–d. Also, the condensed plasma within the loop is continuously accelerated from 156 km/s initially on the bottom to nearly 500 km/s at $t = 16{,}000$ s, which leads to a continuously increasing expansion of the loop. Both the compression and acceleration of the plasma are attributed to the Lorentz force provided by the emerging magnetic field.

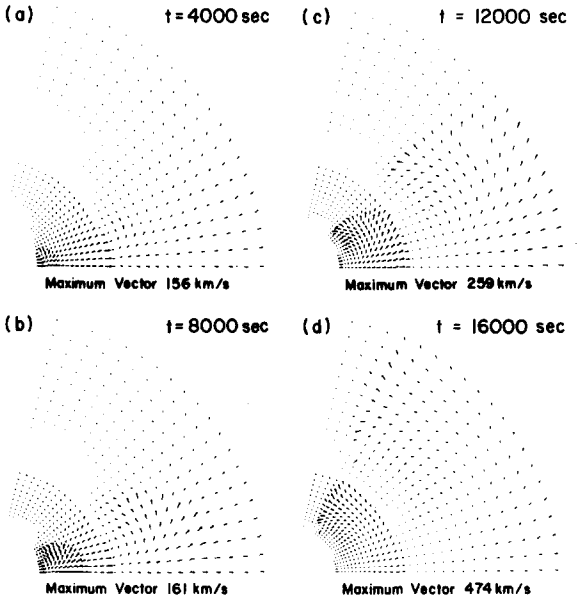

FIG. 6. Velocity distribution at (a) 4000 s, (b) 8000 s, (c) 12,000 s, and (d) 16,000 s.

In addition to the loop structure there is a cavity below and a fast magnetosonic wave in front of it, as well as a low temperature, high density region near the bottom. As expected, the fast wave has been smoothed to some extent owing to the numeric diffusion of the code, with a maximum relative enhancement of density $0.7 \sim 0.8$. The density has a minimum of nearly one-fifth of the background in the cavity and a maximum of 33 times the background near the bottom at $t = 16{,}000$ s. These results illustrate how the magnetic field interacts and dominates the plasma motion.

4. Numerical Test of the Non-reflecting Boundary Condition

As we know, the solar atmosphere has no border at the top but one must introduce an artificial boundary to limit the computation domain. Besides, although the polar axis might be conveniently taken as a symmetric boundary for 2-dimensional problems, one would hope to have the flexibility to choose any latitude as an artificial boundary. Fortunately, we are able to use the projected characteristic method to handle all artificial boundaries, either the top ($r = r_m$) or the left side ($\theta = \theta_0$).

A numerical test of the projected characteristic method was made previously for the top of the domain in Cartesian coordinates [5], and it was demonstrated that this method produces much smaller reflections and affords better accuracy than do other common methods, such as equi-value or linear extrapolation. We will now show that this method works equally well both for the top and for the left side, even though the coordinate system and the difference scheme differ from those in the original test.

First, let us take a look at the top boundary to see how the projected characteristic method works. To this end we limit the computation to a small domain with $r_m = 2.375\ R_\odot$ and then compare the result with the solution obtained for the original domain, as shown in Fig. 7. Figures 7d–f demonstrate the same solution for the density enhancement as do Figs. 4a–c, except that they are rotated by 180° in the horizontal plane. In addition, only the distribution in the small domain is plotted for convenience of comparison. The boundary condition on the top should not exert any significant influence on the large domain solution since the fast magnetosonic wave does not reach the top until $t = 12{,}000$ s. Therefore, it may serve as a standard for classifying the errors of the solution for the small domain (cf. Figs. 4a–c) due to the top boundary condition. Obviously, there is not any appreciable deviation between these two solutions until $t = 8000$ s, even though the fast magnetosonic wave has already passed the top of the small domain some time ago. This means that the present boundary condition allows a smooth passage of low-amplitude waves. At $t = 12{,}000$ s, when the high density loop reaches the top, the reflection does take place, and the boundary condition becomes inapplicable. In the meantime, the identical boundary condition on the left-hand side produces no reflection because the mass loop has not arrived at it yet. This behavior is in accord with the comments of Gustafsson and Kreiss [16], who noted that any charac-

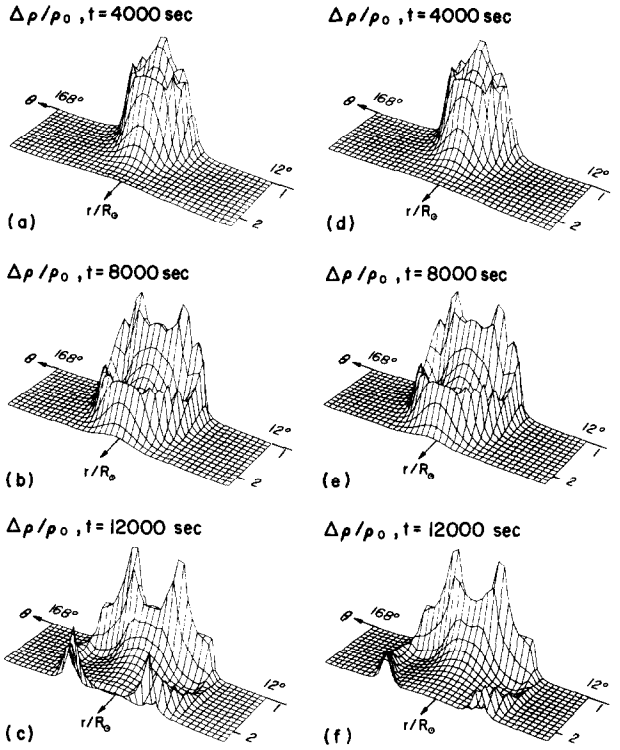

FIG. 7. The effect of top boundary condition on the density enhancement at (a) 4000 s, (b) 8000 s, and (c) 12,000 s with the corresponding standard solutions as shown in (d)–(f).

teristic method for specifying boundary conditions can be effective only for a physical field which changes slowly with respect to space and time outside the boundary. Such a prerequisite does not hold when a disturbance with a steep gradient or discontinuity reaches the boundary. One must then either expand the domain or stop the computation before the reflection becomes appreciable.

Next, to test whether the present boundary condition for the left side ($\theta = \theta_0 > 0$) works as well as a symmetrical condition for the polar axis ($\theta = 0$), we have made computations for the two domains with $\theta_0 = 12°$ and $\theta_0 = 0°$, without introducing any disturbance on the bottom, and then we have compared the two set of results with the initial state, which is determined analytically by Eq. (27). The deviations, if any, must be numerical errors since the initial state will remain in equilibrium if no external disturbance has been introduced. These errors may be attributable to three sources: (1) the boundary condition, (2) the numeric scheme, and (3) the initial state which satisfies the differential equilibrium equations exactly but not their corresponding finite-difference equations. The calculations show that the errors are characterized by a trend towards stability in several time steps. Table I gives the maximum errors of all quantities at $t = 10{,}000$ s which are about the same

TABLE I17.7

Comparison of Maximum Numerical Errors for Different Boundary Conditions

Boundary condition	Projected characteristic	Symmetrical
$\lvert\Delta\rho\rvert/\rho_0$	0.1034	0.1027
$\lvert v_r\rvert$ (km/s)	10.0	17.7
$\lvert v_\theta\rvert$ (km/s)	8.24	8.25
$\lvert\Delta\psi\rvert/(\psi_{0_{max}}-\psi_{0_{min}})$	0.103	0.103
$\lvert\Delta T\rvert/T_0$	0.044	0.045

in the order of magnitude for the two types of boundary conditions. This tells us that the projected characteristic boundary condition has little bearing on the errors and therefore it is really acceptable. Moreover, similar calculations were performed for the case with disturbance introduced on the bottom, and the two sets of results have no appreciable deviation up to $t = 20{,}000$ s, by which time the loop structure has not yet reached the left side ($\theta = 12°$).

V. Accuracy

For a uniform mesh, the present code has a formal accuracy of second order [3] and the artificial diffusion does not affect the truncation error of the difference scheme since it is of third order [4]. Yet a high formal accuracy does not necessarily result in a high real accuracy. Because it is difficult to assess the real accuracy of any code, one is often content with applications to simple problems for which some exact solutions are available. Actually, we have done that at the end of last section where we used an equilibrium as the initial state and did not introduce any disturbances on the bottom. The errors shown in Table I may provide us a conservative estimation of the accuracy of the code: the error velocity ~ 10 km/s and the relative errors of other quantities $\sim 10\%$ after 10^4 s of computation, since any real disturbance will generally suppress such numeric errors.

In what follows, we will further apply the code to numerically reproduce one of the elegant self-similar solutions developed by Low [17] (cf. Eqs. (17)–(22) and Figs. 1–3 in Section II of [17]). This solution is characterized by a purely radial inertial flow with the spatial distribution of the dependent variables remaining similar to itself at all times during the motion. Taking $t = 4t_0$ as the initial time, the computation continues for a physical time of 2×10^4 s wich corresponds to $5.4t_0$, where $t_0 \sim 3700$ s is the characteristic time scale for the self-similar solution. In addition, the initial velocity changes linearly with r from 65 to 390 km/s in Low's model. The maximum errors during this period are listed in Table II. It can be seen that the accuracy here seems better than that for the above disturbance-free case, as expected.

TABLE II

Maximum Numerical Errors in Reproducing a Self-Similar Solution

Physical time (s)	4000	8000	12000	16000	20000
$\lvert\Delta\rho\rvert/\rho$	0.0125	0.0333	0.0451	0.0572	0.0652
$\lvert\Delta v_r\rvert$ (km/s)	3.01	4.07	4.50	4.69	5.48
$\lvert\Delta v_\theta\rvert$ (km/s)	0.70	0.97	0.89	0.84	0.77
$\lvert\Delta\psi\rvert/\psi_{\text{equator}}(\times 10^{-3})$	0.60	0.97	2.0	3.1	2.7
$\lvert\Delta T\rvert/T(\times 10^{-3})$	4.7	6.7	8.4	10.1	11.1

In summary, we would suggest that the present code should give a reasonably reliable result for a transient phenomenon with relative accuracy in the perturbations of about 10% and an error in the disturbance velocity of the order of 10 km/s. The accuracy as well as the applicability of the code will be more sharply defined as more examples are tested in the future.

VI. Numerical Stability Criteria

As a matter of fact, Eq. (23) in Section 3 serves as a stability criterion for using the projected characteristic method on the artificial boundaries. Also, there are certain criteria for the scheme since it is not absolutely stable. One can expect that an implicit scheme will allow a larger time step than would be possible with explicit methods. For the present scheme we introduce an additional constraint on the time step

$$\Delta t < \Delta t_2 = C \cdot \min\left(\frac{\Delta l}{v_a}\right), \tag{30}$$

where C is a constant adjusted by a trial-and-error method, Δl is the grid spacing, and v_a is the Alfven speed. This criterion is much more stringent than Eq. (23) for strong magnetic field cases, since it involves the Alfven time scale. It is found that the computation is stable for $C \leqslant 4$, namely a time step nearly quadrupole of that stipulated by the CFL condition for an explicit method. It seems that this time step is hardly long enough to make the present code more efficient than an explicit scheme. Nevertheless, the main object of this code lies not only in the efficiency, but also in the stability for long time computations. Usually, explicit schemes are apt to become unstable after any part of the boundary gets involved with wave motions, whereas the present code may well avoid such instability.

We would like to emphasize the enhanced stability stemming from the averaging procedure in the third step of the scheme mentioned in Section 2. Eliminating this step results in numerical instability even when the condition (30) is met. For

problems involving a moderate magnetic field, the conventional ADI techniques seem passable but some ripples in numerical results may still appear for a long time computation.

APPENDIX

The governing equations (2) are rewritten as

$$\frac{\partial U}{\partial t}+F\frac{\partial U}{\partial r}+\frac{G}{r}\frac{\partial U}{\partial \theta}=H, \tag{A1}$$

where H is the vector of inhomogeneous terms, and F and G are 5×5 matrices given by

$$F=\begin{pmatrix} v_r & \rho & 0 & 0 & 0 \\ \dfrac{RT}{\rho} & v_r & 0 & \dfrac{1}{\rho}L\psi & R \\ 0 & 0 & v_r & 0 & 0 \\ 0 & 0 & 0 & v_r & 0 \\ 0 & (\gamma-1)T & 0 & 0 & v_r \end{pmatrix} \tag{A2}$$

and

$$G=\begin{pmatrix} v_\theta & 0 & \rho & 0 & 0 \\ 0 & v_\theta & 0 & 0 & 0 \\ \dfrac{RT}{\rho} & 0 & v_\theta & \dfrac{1}{\rho}L\psi & R \\ 0 & 0 & 0 & v_\theta & 0 \\ 0 & 0 & (\gamma-1)T & 0 & v_\theta \end{pmatrix}. \tag{A3}$$

1. *For r–t Plane*

The left eigenvectors of F, ξ_μ, are defined by

$$\xi_\mu \cdot F=\lambda_\mu \xi_\mu \qquad (\mu=1, ..., 5), \tag{A4}$$

where the eigenvalues λ_μ are easily found to be

$$\lambda_\mu = v_r, \qquad v_r \pm c_s \tag{A5}$$

and the corresponding eigenvectors ξ_μ are listed in Table A1. Note that v_r is a triple eigenvalue and therefore, there are three independent eigenvectors associated with it.

TABLE A1

Eigenvalues and Eigenvectors for F

λ	ξ
$v_r - c_s$	$(RT, -\rho c_s, 0, L\psi, \rho R)$
v_r	$((\gamma-1)T, 0, 0, 0, -\rho)$
v_r	$(0, 0, 1, 0, 0)$
v_r	$(0, 0, 0, 1, 0)$
$v_r + c_s$	$(RT, \rho c_s, 0, L\psi, \rho R)$

Finally, the projected characteristic equations along them are expressed by

$$\frac{dr}{dt} = v_r, \qquad v_r \pm c_s, \tag{A6}$$

and

$$\xi_\mu \cdot \left(\frac{\partial U}{\partial t} + W\right) = 0. \tag{A7}$$

2. *For $\theta - t$ Plane*

In a similar way we may derive the projected characteristics and their associated characteristic equations starting from

$$\eta_v \cdot G = \sigma_v \eta_v \qquad (v = 1, ..., 5), \tag{A8}$$

and the results are

$$r\frac{d\theta}{dt} = \sigma_v = v_\theta, \qquad v_\theta \pm c_s \tag{A9}$$

and

$$\eta_v \cdot \left(\frac{\partial U}{\partial t} + W\right) = 0, \tag{A10}$$

where the eigenvectors η_v are listed in Table A2.

TABLE A2

Eigenvalues and Eigenvectors for G

σ	η
$v_\theta - c_s$	$(RT, 0, -\rho c_s, L\psi, \rho R)$
v_θ	$(0, 1, 0, 0, 0)$
v_θ	$((\gamma-1)T, 0, 0, 0, -\rho)$
v_θ	$(0, 0, 0, 1, 0)$
$v_\theta + c_s$	$(RT, 0, \rho c_s, L\psi, \rho R)$

TABLE A3

Classification of Projected Characteristics

v_n	Outgoing	Incoming
$v_n \leqslant -c_s$	$-(0)$	$v_n, v_n \pm c_s$ (5)
$-c_s < v_n < 0$	$v_n + c_s$ (1)	$v_n, v_n - c_s$ (4)
$0 \leqslant v_n < c_s$	$v_n, v_n + c_s$ (4)	$v_n - c_s$ (1)
$v_n \geqslant c_s$	$v_n, v_n \pm c_s$ (5)	$-(0)$

We point out in passing that (A7) or (A10) serve as compatibility relations as long as the characteristics corresponding to ξ_μ or η_ν are ascertained to be outgoing for a boundary in question.

As mentioned in Section 2, the non-reflecting boundary conditions are given by

$$\xi_\mu \cdot \frac{\partial U}{\partial t} = 0 \tag{A11}$$

or

$$\eta_\nu \cdot \frac{\partial U}{\partial t} = 0, \tag{A12}$$

provided the projected characteristics associated with ξ_μ and η_ν are incoming. The criteria for identifying a projected characteristic with incoming or outgoing are listed in Table A3, where v_n is the external normal velocity on the boundary and the figures in the parentheses denote the number of characteristics.

ACKNOWLEDGMENTS

The paper was prepared during my visit at the High Altitude Observatory. I owe special thanks to Boon Chye Low for beneficial discussions and to Vic Pizzo for reading and commenting on this paper. I am also grateful to Bob MacQueen, Grant Athay, and Peter Gilman for their hospitality.

REFERENCES

1. F. H. HARLOW AND A. A. AMSDEN, *J. Comput. Phys.* **3**, 80 (1968).
2. F. H. HARLOW AND A. A. AMSDEN, *J. Comput. Phys.* **8**, 197 (1971).
3. I. LINDEMUTH AND J. KILLEEN, *J. Comput. Phys.* **13**, 181 (1973).
4. D. SCHNACK AND J. KILLEEN, *J. Comput. Phys.* **35**, 110 (1980).
5. Y. Q. HU AND S. T. WU, *J. Comput. Phys.* **55**, 33 (1984).
6. S. T. WU, Y. Q. HU, S. WANG, M. DRYER, AND E. TANDBERG-HANSSEN, *Astrophys. Space Sci.* **83**, 189 (1982).
7. S. T. WU, Y. Q. HU, Y. NAKAGAWA, AND E. TANDBERG-HANSSEN, *Astrophys. J.* **266**, 866 (1983).
8. S. T. WU, Y. Q. HU, K. KRALL, M. J. HAGYARD, AND J. B. SMITH, JR., *Solar Phys.* **90**, 117, (1984).

9. S. T. WU, Y. Q. HU, Y. NAKAGAWA, AND E. TANDBERG-HANSSEN, *Astrophys. J.* **306**, 751 (1986).
10. A. LAPIDUS, *J. Comput. Phys.* **2**, 154 (1967).
11. Y. Q. HU, *Sci. Sinica* **29**, 199 (1986).
12. Y. Q. HU AND S. P. JIN, in *International Symposium of Space Physics, Beijing, China, November 11-14, 1986; Chinese J. Space Sci.* **7**, 1 (1987).
13. B. C. LOW, *Astrophys. J.* **310**, 953 (1986).
14. D. N. RUST, *Solar Phys.* **25**, 141 (1972).
15. Y. UCHIDA AND T. SAKURAI, *Solar Phys.* **51**, 413 (1977).
16. B. B. GUSTAFSSON AND H. O. KREISS, *J. Comput. Phys.* **30**, 333 (1979).
17. B. C. LOW, *Astraphys. J.* **281**, 392 (1984).